

Dynamics of electron injection in a laser-wakefield accelerator

J. Xu, A. Buck, S.-W. Chou, K. Schmid, B. Shen, T. Tajima, M. C. Kaluza, and L. Veisz

Citation: [Physics of Plasmas](#) **24**, 083106 (2017); doi: 10.1063/1.4996906

View online: <https://doi.org/10.1063/1.4996906>

View Table of Contents: <http://aip.scitation.org/toc/php/24/8>

Published by the [American Institute of Physics](#)

Articles you may be interested in

[Ultrafast multi-MeV gamma-ray beam produced by laser-accelerated electrons](#)
[Physics of Plasmas](#) **24**, 093104 (2017); 10.1063/1.4996020

[Generation of 20 kA electron beam from a laser wakefield accelerator](#)
[Physics of Plasmas](#) **24**, 023108 (2017); 10.1063/1.4975613

[Intense \$\gamma\$ ray generated by refocusing laser pulse on wakefield accelerated electrons](#)
[Physics of Plasmas](#) **24**, 093110 (2017); 10.1063/1.4994710

[Laser beam coupling with capillary discharge plasma for laser wakefield acceleration applications](#)
[Physics of Plasmas](#) **24**, 083109 (2017); 10.1063/1.4997606

[Temporal profile of betatron radiation from laser-driven electron accelerators](#)
[Physics of Plasmas](#) **24**, 063107 (2017); 10.1063/1.4985687

[Optimization and control of electron beams from laser wakefield accelerations using asymmetric laser pulses](#)
[Physics of Plasmas](#) **24**, 103101 (2017); 10.1063/1.5001849

PHYSICS TODAY

WHITEPAPERS

ADVANCES IN PRECISION
MOTION CONTROL

Piezo Flexure Mechanisms
and Air Bearings

READ NOW

PRESENTED BY

PI

Dynamics of electron injection in a laser-wakefield accelerator

J. Xu,^{1,2,a)} A. Buck,^{1,3} S.-W. Chou,¹ K. Schmid,^{1,3} B. Shen,² T. Tajima,⁴ M. C. Kaluza,^{5,6} and L. Veisz^{1,7,a)}

¹Max-Planck-Institut für Quantenoptik, Hans-Kopfermann-Strasse 1, 85748 Garching, Germany

²State Key Laboratory of High Field Laser Physics, Shanghai Institute of Optics and Fine Mechanics, Chinese Academy of Sciences, P. O. Box 800-211, Shanghai 201800, China

³Ludwig-Maximilians-Universität München, Am Coulombwall 1, 85748 Garching, Germany

⁴Department of Physics and Astronomy, University of California, Irvine, California 92697, USA

⁵Institute of Optics and Quantum Electronics, Max-Wien-Platz 1, 07743 Jena, Germany

⁶Helmholtz-Institute Jena, Fröbelstieg 3, 07743 Jena, Germany

⁷Department of Physics, Umeå University, SE-901 87 Umeå, Sweden

(Received 24 May 2017; accepted 18 July 2017; published online 1 August 2017)

The detailed temporal evolution of the laser-wakefield acceleration process with controlled injection, producing reproducible high-quality electron bunches, has been investigated. The localized injection of electrons into the wakefield has been realized in a simple way—called shock-front injection—utilizing a sharp drop in plasma density. Both experimental and numerical results reveal the electron injection and acceleration process as well as the electron bunch's temporal properties. The possibility to visualize the plasma wave gives invaluable spatially resolved information about the local background electron density, which in turn allows for an efficient suppression of electron self-injection before the controlled process of injection at the sharp density jump. Upper limits for the electron bunch duration of 6.6 fs FWHM, or 2.8 fs (r.m.s.) were found. These results indicate that shock-front injection not only provides stable and tunable, but also few-femtosecond short electron pulses for applications such as ultrashort radiation sources, time-resolved electron diffraction or for the seeding of further acceleration stages. *Published by AIP Publishing.*

[<http://dx.doi.org/10.1063/1.4996906>]

I. INTRODUCTION

Applications of femtosecond (fs) scale relativistic electron bunches require high shot-to-shot stability of operation in laser wakefield acceleration.¹ In the bubble regime,^{2,3} background electrons get trapped in the first plasma period through self-injection^{4–8} when their velocities are high enough to catch up with the rear side of the bubble, but this process strongly depends on the laser intensity evolution and thus the nonlinear development of the plasma wave.^{9–11} The breaking of the plasma wave, initiating the electron injection, can be reached in a controlled way when the wave amplitude is highly relativistic but still below the threshold for self-injection. In this case, the position where electron injection occurs is localized leading to a more stable and reproducible output of high-energy electron bunch than in the self-injection case. Various techniques have been proposed and experimentally demonstrated to realize controlled electron injection and to stabilize the electron bunch output. One of these methods is applying a secondary counter-propagating laser pulse to pre-accelerate a fraction of the background electrons to moderate energies. These pre-accelerated electrons then have high-enough momenta to catch up with the bubble end.^{12,13} Another approach is ionization injection using a gas mixture that produces electron bunches with a broad energy spectrum suitable as an injector for cascaded acceleration.^{14,15} In the gradual density down-ramp scheme,^{16,17} the

decreasing bubble velocity allows for the trapping of electrons in the bubble. However, this injection process is active over a certain duration and hence leads to a large energy spread of the output electrons. A recent experiment shows that a structured density profile between the dual-stage gas jet compresses the energy spread to 1%.¹⁸

We realized controlled electron injection in a simple but practical way *via* the so-called “shock-front injection” scheme, based on a sharp density jump,¹⁹ to precisely localize and limit the injection of background plasma electrons to a region of a few micrometer length only.²⁰ This process is triggered by a sharp density drop, which originates from a shock front generated in the gas by the knife-edge of a blade mounted above the nozzle to block a part of a supersonic gas flow. Shock-front injection was applied successfully with various laser pulse durations of sub-5 fs, 8 fs, and 26 fs at different laser intensities in a large density range of 10^{18} cm^{-3} to $2 \times 10^{20} \text{ cm}^{-3}$.^{21,22} The fs output electron bunch has a stable and tunable energy from few MeV to 150 MeV, which can be increased even to the GeV energy level when applying even lower plasma densities, and a small absolute energy spread of 3–5 MeV. A stable few MeV electron bunch has great potential for application in ultrafast electron diffraction and as a reliable injector for staged electron acceleration.^{23,24} The generation of stable fs electron bunches with tunable energies also produced ultra-bright coherent x-ray radiation pulses.^{25–27} However, to understand this unique injection mechanism and to further develop it, a detailed study with direct experimental insight

^{a)}Authors to whom correspondence should be addressed: jxu@siom.ac.cn and laszlo.veisz@umu.se

is needed. Here, an optical probe pulse with few-fs duration used in a transverse probing geometry would be required both to resolve the electron bunch *via* its magnetic field as well as the plasma wave.

In this letter, experimental investigations of the dynamics of shock-front injection and the following acceleration process of the electron bunch as well as the evolution of the plasma wave are presented by combining “time-resolved polarimetry”^{28,29} and “plasma shadowgraph of the two techniques.”³⁰ The larger part of a few-cycle laser pulse, in particular with a pulse duration shorter than half of the plasma period, drives the acceleration process while a second, low energy portion of the laser pulse probes the interaction region with a high spatial and few-fs temporal resolution. It allows observing the time evolution of the electron bunch as well as the plasma wave for the whole interaction process.^{31,32} Therefore, it provides a direct insight into the injection and acceleration process of the shock-front-injected electron bunch.

II. EXPERIMENTAL SETUP

The experiments were performed with the multi-TW 8-fs full-width-at-half-maximum (FWHM) laser system, Light Wave Synthesizer 20 (LWS-20).³³ It delivered 130 mJ at the end of the laser chain and 65 mJ on the target in the main beam and 2 mJ in the probe beam. The experimental setup is shown in Fig. 1(a). An $f/10$ off-axis parabolic mirror (OAP) focused the main beam to an 11.7- μm FWHM spot with an intensity of $1.2 \times 10^{18} \text{W}/\text{cm}^2$ into a helium gas jet, which was emanating from a supersonic nozzle with an exit diameter of 300 μm . A gas shock front with a width of Δz , as shown in Fig. 1(b), originating from a razor blade above the nozzle produced a sharp downward density transition, which initiated shock-front injection. The produced high-energy electrons propagated through a high-resolution focusing permanent-magnet spectrometer covering a broad energy range of 2.5–400 MeV (Ref. 34) and were detected by scintillating screens (Kodak Biomax) imaged to a 12-bit CCD camera. There was a 20- μm thick aluminum foil in front of the spectrometer to block the laser pulses. Quasimonoenergetic electron bunches with a peak energy of $20.8 \pm 0.4 \text{ MeV}$ and a total charge of $2.80 \pm 0.22 \text{ pC}$, were observed, as shown in Fig. 1(c).

The electron bunch position and duration were measured by applying the time-resolved polarimetry technique. The relativistic electron bunch generates an azimuthal magnetic field B_ϕ around itself. The probe beam, propagated through the interaction area perpendicular to the main beam to take snapshots of the interaction process at variable times, is controlled by the pump-probe delay. The probe polarization was rotated by the Faraday effect induced by the magnetic field B_ϕ in the probe propagation direction in the plasma medium. Based on Refs. 29 and 32, the rotation angle is $\varphi_{\text{rot}} \propto \int n_e \vec{B}_\phi d\vec{s}$, where l is the propagation path of the probe beam through the interaction area and n_e is the local plasma density. The polarization rotation of the short probe beam was measured in a spatially resolved way containing the information about the electron bunch. There are additional magnetic fields inside the accelerating plasma bubble induced by the displacement current. However, under our experimental conditions their amplitudes are several times weaker than B_ϕ and therefore they are negligible as also confirmed by the simulations presented below.

The probe-beam imaging system contained a long-working-distance microscope objective ($10\times$, $f = 20 \text{ mm}$, Mitutoyo) combined with an achromatic lens ($f = 250 \text{ mm}$). The experimentally determined resolution was $(2.0 \pm 0.1) \mu\text{m}$. The probe beam was divided into two beams by a non-polarizing beam splitter after the lens which imaged the interaction area onto two CCD cameras (Point Grey). Two Glan-laser polarizers were inserted in front of the cameras, detuned by an angle of $\theta_{\text{pol},1} = +7^\circ$ and $\theta_{\text{pol},2} = -7^\circ$ relative to the maximum attenuation, respectively. The detuning allows the determination of the sign of the magnetic field. The extinction ratio of the arrangement in the two arms ($E_{R,i}$, $i = 1, 2$) depended on the initial probe beam polarization state as only one polarizer was in the beam path. The polarization contrast $\beta_i = 1 - 1/E_{R,i}$ was measured to be $\beta_1 = 0.9920 \pm 0.0008$ and $\beta_2 = 0.9767 \pm 0.0033$ as described below. The intensity on the two cameras is expressed as $I_{\text{pol},i}(y,z) = I_0(y,z) \cdot T_i \cdot [1 - \beta_i \times \cos^2(\varphi_{\text{rot}}(y,z) - \theta_{\text{pol},i})]$, where $I_0(y,z)$ is the initial intensity of the probe beam and T_i is the transmission through/reflection of the beam splitter. The absolute scale of $\theta_{\text{pol},i}$ and the values of β_i are obtained when $\varphi_{\text{rot}}(y,z) = 0$, i.e., without plasma, by one full rotation of the

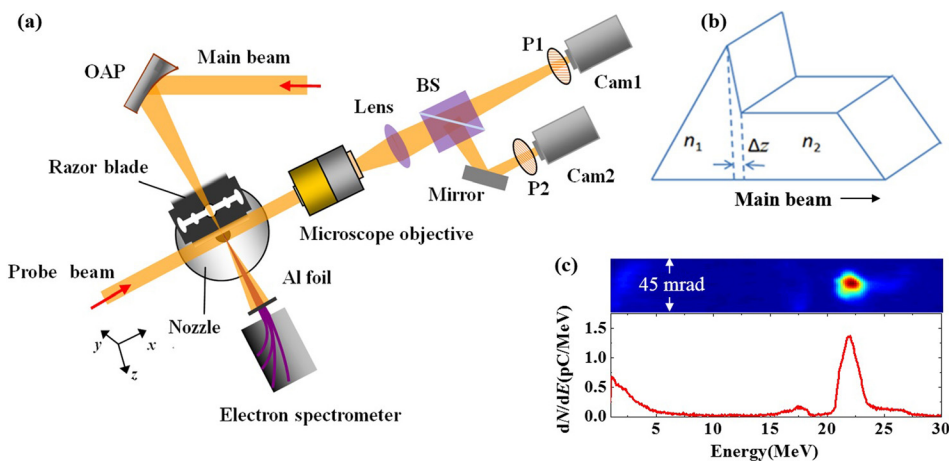


FIG. 1. (a) Experimental setup. P1, P2: Glan-laser polarizers; OAP: off-axis parabolic mirror; BS: non-polarizing beam splitter; Cam1, Cam2: CCD cameras. A razor blade was mounted above the gas nozzle, which blocks a part of gas flow and generates a special density profile. (b) Sketch of the gas density profile: the density rapidly increases in region n_1 , and it drops afterwards to n_2 over a very short transition length Δz . In the n_2 region, the gas density is not affected by the blade. (c) A typical energy spectrum of output electrons.

polarizers and measuring the signal at the same time. The ratio T_1/T_2 is determined from the average intensity ratio of two pictures with maximal signal ($\theta_{\text{pol},i}=90^\circ$) and without polarization rotation ($\varphi_{\text{rot}}(y,z)=0$). After this pre-calibration, the ratio $I_1(y,z)/I_2(y,z)$ only depends on the rotation angle $\varphi_{\text{rot}}(y,z)$ and it is monotonic over a larger range than the measured values due to our choice of the values of $\theta_{\text{pol},i}$. With careful background subtraction and correct overlap of two images from the cameras [Cam1 and Cam2 in Fig. 1(a)], the rotation signal of the electron bunch is determined.

The refraction of the probe beam by the periodic electron density gradient of the plasma wave leads to an intensity modulation in the image plane, i.e., on the two high-resolution cameras. The probe beam duration of 8 fs is half of the plasma period for the background density of $4.8 \times 10^{19} \text{ cm}^{-3}$, which was used in our experiments, and the depth of focus of the objective is $4.1 \mu\text{m}$, comparable to the transversal size of the plasma wave, which is approximately the plasma wavelength. Therefore, the contrast of the intensity modulation is reduced, but not washed out completely. The measured intensity modulation depth is proportional to the electron density gradient, i.e., the plasma wave amplitude. This shadowgraphy method provides the original position, period, and rough amplitude of the wave,³² however, the exact shape of the nonlinear density modulation is smoothed out. In our experiments, the plasma wave is observable simultaneously before and after the shock front for a suitable delay between the probe and main laser pulses.

III. RESULTS AND DISCUSSION

Figures 2(a) and 2(b) show the background subtracted images of Camera 1 at two different delay values corresponding to approximately $z = 15 \mu\text{m}$ and $z = 95 \mu\text{m}$ main pulse positions behind the shock front, which is the slightly tilted vertical line. The background is obtained by averaging the signal over all shots in the delay scan. Plasma wave periods before as well as after the shock front are visible. The z -axis corresponds to the laser propagation direction, and the zero longitudinal position is at the end of density jump region at the laser propagation axis, which is also the zero y

coordinate. The shock front in the figure is modulated and the image shows several parallel lines because the strongly diffracted parts of the probe by the sharp density transition, i.e., the index of refraction transition, are interfering with its other non-diffracted portions. Note that the shock front generated by the razor blade extends over a range much wider than the depth of focus of our imaging system. The sharp density jump forms just above the blade. The density ratio before and after the jump remains approximately constant over a large vertical range of a few hundred μm , and the laser pulse is focusable quite close to the blade, if necessary. A limited vertical range of the sharp density jump is shown here, which originates from the shock front in the supersonic gas jet with a transition width of $\Delta z = 2.5 \mu\text{m}$, measured with Rayleigh scattering $225 \mu\text{m}$ above the blade, which is positioned $100 \mu\text{m}$ above the nozzle. The constant amplitude of the plasma wave over many plasma periods in Fig. 2(b) indicates that this acceleration scenario, in fact, is far from the strongly nonlinear regime with self-injection.

In front of the density jump, i.e., in the n_1 density region, the plasma wavelength gets gradually shorter along the laser propagation axis, which indicates a rapidly increasing plasma density before the shock front ($\lambda_p \propto 1/\sqrt{n(z)}$). Through plasma wavelength data analysis of tens of shots we obtain the local electron density profile in the longitudinal direction as shown in Fig. 2(c). The electron density increases from 5.6 to $8.7 \times 10^{19} \text{ cm}^{-3}$ in $50 \mu\text{m}$ approx. linearly, which is in good agreement with former interferometric results.²⁰

In homogenous plasma, the bubble propagates with the same velocity as the driving laser pulse. However, in the case of rapidly increasing density the plasma period also shrinks fast while the bubble front propagates along with the same velocity as the group velocity of the laser pulse. Correspondingly, the bubble end propagates faster than the laser pulse and hence completely inhibits self-injection of background electrons. Here the energy depletion of the laser is negligible over a distance of $50 \mu\text{m}$ and therefore etching of the leading edge of laser pulse front is not relevant over these length scales. To investigate this in more detail, we calculate the phase velocity of the bubble end³⁵

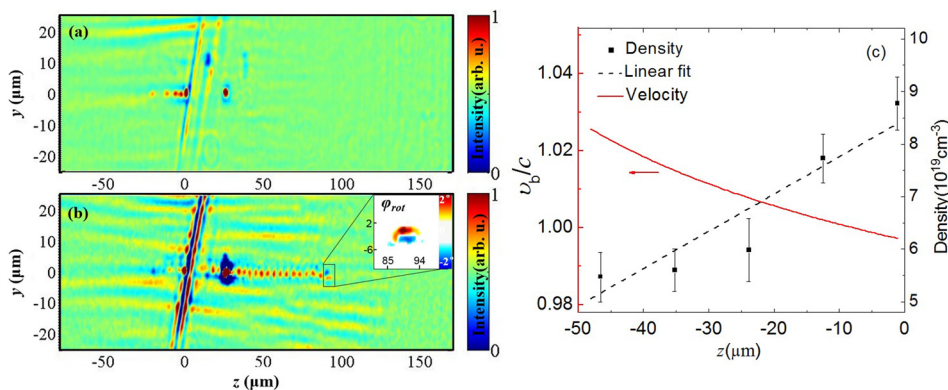


FIG. 2. Plasma oscillations from a background subtracted image taken with camera 1 with different positions of the main beam at (a) $15 \mu\text{m}$ and (b) $95 \mu\text{m}$, inset: Faraday signal deduced from the image from both cameras. (c) Electron density before the shock front calculated from the plasma wavelength based on shadowgram snapshots (black squares), linear fit to density curve (black dashed line), and the estimated velocity of the rear side of the bubble (red solid line). This velocity is larger than the speed of light in vacuum, which indicates that electron self-injection before the shock front does not take place.

$$v_b = v_g + v_{sh} \approx \frac{1 - \frac{n(z)}{2\gamma_a n_{cr}}}{1 + \lambda_L \frac{d\sqrt{\gamma_a n_{cr}/n(z)}}{dz}} c,$$

where v_g is the group velocity of the laser pulse, v_{sh} is the shrinking speed of the bubble size, c is the speed of light in vacuum, $n(z)$ is the background electron density, n_{cr} is the critical density at the central laser wavelength of $\lambda_L = 800$ nm, and $\gamma_a \approx \sqrt{1 + a_0^2/2}$ is the γ -factor averaged over the electron distribution, which depends on the normalized vector potential of the laser a_0 for linear polarization. Figure 2(c) plots the calculated phase velocity of the bubble end v_b , which mostly exceeds the speed of light in vacuum before the shock front. Therefore, the background electrons assemble at the bubble end and form a density peak with high forward momentum but they cannot be injected into the accelerating region and trapped inside even though the high laser intensity drives a nonlinear plasma wave.³⁶

Electron injection is triggered, however, the rapid density drop after this position and in addition to the plasma wave, the electron bunch has been observed experimentally. The inset in Figure 2(b) shows the polarization rotation angle deduced from the ratio of the two camera images.³² This signal from polarization rotation in camera 1 is at the head of the plasma wave at $z = 90.6 \mu\text{m}$; it indicates that the trapped electron bunch sits in the first plasma-wave period. We detected the electron bunch as well as the plasma wave at different time delays. The delay between the main beam and the probe beam was tuned by steps of 67 fs, i.e., $20 \mu\text{m}$. We roughly took 60 laser shots for each delay step. The observed plasma wave can be used to measure the local plasma wavelength, which in turn gives the density even time resolved when neglecting relativistic nonlinearities, which seems reasonable for our weakly relativistic intensity. This local plasma density is plotted in Fig. 3(a), which is in reasonable

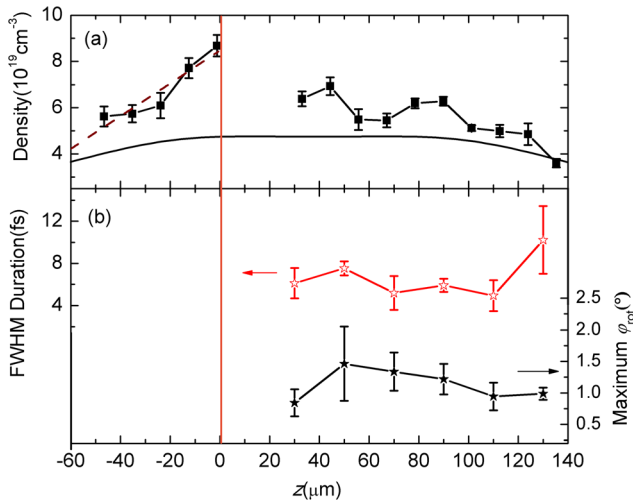


FIG. 3. (a) Electron density deduced from the measured plasma wavelength (solid squares), (b) electron bunch duration (FWHM, red empty stars) and maximum rotation angle $\varphi_{rot,max}$ (black solid stars). Each point is an average over 5–18 laser shots. The dashed line is a linear fit to the electron density before the shock-front position, and the continuous black line is the electron density without the blade measured by interferometry.

agreement with the interferometric result shown as the solid black line. However, a slight systematic increase (about 20%) in the measured density is present. The electron density profile confirms that the gas shock structure was caused by the blade blocking the part of the gas flow.²⁰ Using this method, the output electron bunch energy is easily tunable by moving the blade along the longitudinal axis.²¹

These snapshots allow us to study the injection and acceleration process of injected electrons. The observation of the maximum Faraday rotation angle, plotted in Fig. 3(b), indicates that the electron bunch signal appears $30 \mu\text{m}$ after the shock-front position. However, at the position of $z = 10 \mu\text{m}$, neither a Faraday signal from the electrons nor the plasma wave can be detected, because the strong diffraction from the shock front suppresses these signals. There is no detected magnetic field signal due to an electron bunch before the shock-front position, where the diffraction is lower and the plasma wave is visible. Electrons are not injected before the shock front, which agrees well with the result from the measured density profile as discussed before. The background density is significantly below the lowest density supporting electron self-injection. The observed deconvolved electron bunch duration is also plotted and has an average value of $\tau_{bunch} = 6.6$ fs FWHM or equivalently 2.75 fs root-mean-square. The real pulse duration of the electron bunch is probably shorter than this experimentally measured value due to the limited resolution originating from the 8 fs laser pulse duration and the conservatively applied deconvolution of the measured signal from the Faraday rotation. The maximum rotation angle $\varphi_{rot,max}$, which has a linear relationship with the peak current of the electron bunch, as well as the bunch duration τ_{bunch} stays constant within the error bars indicating that the total charge of the electron bunch ($\propto \varphi_{rot,max} * \tau_{bunch}$) is constant, i.e., there is no subsequent injection after the injection triggered by the shock front. The electrons get injected only at the shock-front position, i.e., only once over the whole interaction length, which is in agreement with the previous arguments about the superluminal velocity of the bubble end before the shock front. This is also confirmed by the single high-quality mono-energetic peak in the output electron spectrum in Fig. 1(c). There are no low-energy background electrons but only one electron energy peak at 20.8 MeV.

Our experimental observations confirm that electron injection occurs only once at the shock-front position. Afterwards the electron bunch charge remains constant, and there is no further injection. The electron bunch sits in the first bubble and gets accelerated to high energies. To further understand the injection process of the electron bunch as well as the dynamics of the plasma wave, three-dimensional simulations have been performed using the Particle-In-Cell (PIC) code VORPAL³⁷ with a macro particle number of $500 \times 300 \times 300$ in a simulation box of $25 \times 30 \times 30 \mu\text{m}^3$. The simulation parameters were set to match the experimental conditions. The plasma density profile has a linear ramp to $n_1 = 8.7 \times 10^{19} \text{cm}^{-3}$ and then drops to $n_2 = 4.8 \times 10^{19} \text{cm}^{-3}$ over a length of $\Delta z = 3 \mu\text{m}$. A laser pulse with a Gaussian temporal profile and $\tau_{FWHM} = 8$ fs was focused at the shock-front position $z = 0$ to a

FWHM spot size of $12\ \mu\text{m}$ reaching a peak normalized vector potential of $a_0 = 1$. Figure 4 plots the plasma wave near the shock-front region as well as the electron bunch at different time steps. The electrons are injected into the first bubble at the shock-front position. When the laser pulse propagates in the high-density n_1 region, the laser pulse drives a plasma wave train and the plasma wavelength shortens rapidly with the longitudinal position. The phase velocity exceeds the speed of light and no electrons can get trapped into the bubble. The electrons form a dense electron peak at the first bubble end that reaches $2 \times 10^{20}\text{cm}^{-3}$, roughly four times higher than the background plasma density. It is clearly visible that there is no electron injection in the high-density n_1 region.

When the laser pulse propagates further, the plasma density drops by a factor of 1.8 over a transition length of $\Delta z = 3\ \mu\text{m}$, which is shorter than the plasma wavelength ($\lambda_p = 4.8\ \mu\text{m}$). The sudden jump of the plasma density causes a correspondingly rapid elongation of the plasma wavelength injecting a huge number of electrons into the now longer first plasma period. As too many electrons are injected into the first bubble, they expel the boundary electrons and prohibit any further injection while they leave. Most of these injected electrons cannot catch up with the bubble and only a small portion of them is trapped subsequently experiencing energy gain. However, some electrons are injected into the subsequent plasma periods due to the lengthening of the plasma wavelength, and the plasma wave amplitude is significantly decreased after the first period due to the energy transfer to the accelerated electrons and the injection phase is also insufficient. After intense plasma dynamics, the electron bunch is formed and accelerated at

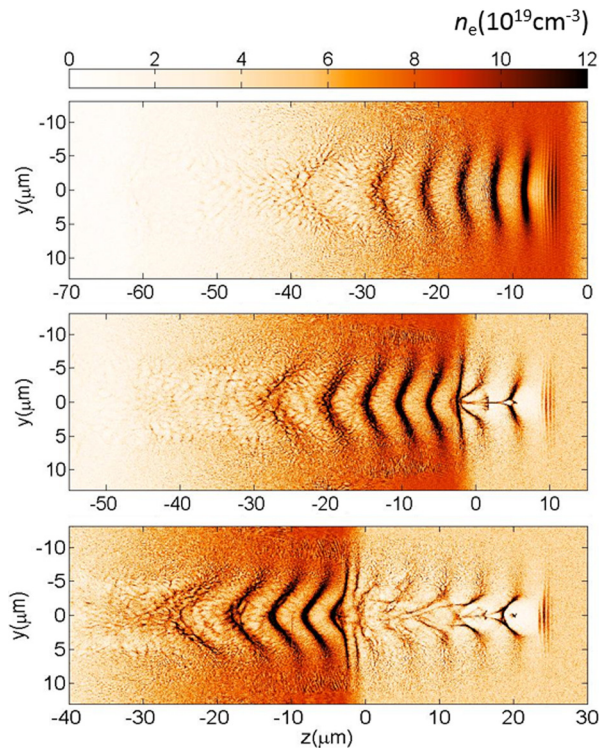


FIG. 4. Electron injection process and plasma wave evolution from 3D PIC simulation.

$z = 20\ \mu\text{m}$. It is clearly visible that the first bubble keeps its background-electron-free cavity and has a high-quality electron bunch accelerated inside. The following bubble train in the low-density n_2 region has quite reduced amplitude in agreement with the experiments.

Electrons trapped in the first bubble will suppress further injection of the background electrons due to the Coulomb repulsion. Therefore, only the accelerated electron bunch in the first bubble will leave the plasma. The shock-front injection produces a single high-quality electron bunch free of low-energy background. The 3D simulation results show that the FWHM pulse duration is only 2.0 fs with a charge of 3.2 pC and a peak electron energy of 23 MeV. The charge and the electron energy agree well with the experiments, but the electron bunch duration is 3 times shorter than the experimentally measured value, which might be due to the limited experimental resolution achievable with 8 fs probe pulses as discussed before. The 3D PIC simulation results indicate that the energy spread of the generated electron bunch depends mainly on the length and weakly on the depth of the plasma density transition. The length of plasma density transition is critical for electron bunch injection and the longer it is the larger the energy spread. If it approaches the plasma wavelength the injection technique does not work, which agrees well with our experimental observation. However, by further increasing the transition length the down ramp injection regime is entered with much less favorable properties. The depth of plasma density transition defines the difference of plasma wavelength before and after the shock position and thus it defines where the electron bunch is injected in the elongated plasma wave as well as influences the injected charge. This charge has a certain influence on the energy spread due to space charge effects. A simple way of reducing it further is to decrease the shock-front width. We had to decrease the shock-front width in our newest experiments with sub-5-fs laser pulse duration to enter the shock-front injection at all. Applying this to longer pulses (and matched lower densities) will naturally provide smaller spread.

IV. CONCLUSION

In conclusion, we have presented a detailed spatial and temporal investigation of electron injection with the shock-front technique. Spatial observation of the plasma wave revealed (1) a rapid density increase before the shock front, which suppressed early electron injection; (2) a long homogeneous plasma wave indicating that the process was far from the strongly nonlinear regime. Temporal measurements supported the few-fs bunch duration that is constant during acceleration and a single injection at/after the shock front. These results pave the way for applications of fs-scale, stable, and energy tunable high-quality electron bunches as for example, ultrashort radiation sources, probes of ultrafast processes or seed pulses for further acceleration stages.

ACKNOWLEDGMENTS

We would like to thank Dr. C. M. S. Sears for useful discussions. This work was supported by the DFG-Project Transregio TR18, by the Euratom research and training

program 2014–2018 under grant agreement No 633053 within the framework of the EUROfusion Consortium and by The Munich Centre for Advanced Photonics (MAP). L. V. acknowledges the support by a grant from the Swedish Research Council (2016-05409). J. Xu would like to thank the support by the Max Planck Society (MPS)-Chinese Academy of Sciences (CAS) Joint Doctoral Promotion Program and the National Natural Science Foundation of China (Project No. 11505264).

- ¹T. Tajima and J. M. Dawson, *Phys. Rev. Lett.* **43**, 267 (1979).
- ²A. Pukhov and J. Meyer-ter-Vehn, *Appl. Phys. B* **74**, 355 (2002).
- ³W. Lu, M. Tzoufras, C. Joshi, F. S. Tsung, W. B. Mori, J. Vieira, R. A. Fonseca, and L. O. Silva, *Phys. Rev. Spec. Top. Accel. Beams* **10**, 061301 (2007).
- ⁴N. A. M. Hafz, T. M. Jeong, I. W. Choi, S. K. Lee, K. H. Pae, V. V. Kulagin, J. H. Sung, T. J. Yu, K.-H. Hong, T. Hosokai, J. R. Cary, D.-K. Ko, and J. Lee, *Nat. Photonics* **2**, 571 (2008).
- ⁵X. Wang, R. Zgadzaj, N. Fazel, Z. Li, S. A. Yi, X. Zhang, W. Henderson, Y.-Y. Chang, R. Korzekwa, H.-E. Tsai, C.-H. Pai, H. Quevedo, G. Dyer, E. Gaul, M. Martinez, A. C. Bernstein, T. Borger, M. Spinks, M. Donovan, V. Khudik, G. Shvets, T. Ditmire, and M. C. Downer, *Nat. Commun.* **4**, 1988 (2013).
- ⁶S. Corde, A. Thaur, C. Lifschitz, G. Lambert, K. Ta. Phuoc, X. Davoine, R. Lehe, D. Douillet, A. Rousse, and V. Malka, *Nat. Commun.* **4**, 1501 (2013).
- ⁷W. P. Leemans, A. J. Gonsalves, H.-S. Mao, K. Nakamura, C. Benedetti, C. B. Schroeder, C. Tóth, J. Daniels, D. E. Mittelberger, S. S. Bulanov, J.-L. Vay, C. G. R. Geddes, and E. Esarey, *Phys. Rev. Lett.* **113**, 245002 (2014).
- ⁸S. Y. Kalmykov, A. Beck, S. A. Yi, V. N. Khudik, M. C. Downer, E. Lefebvre, B. A. Shadwick, and D. P. Umstadter, *Phys. Plasmas* **18**, 056704 (2011).
- ⁹E. Esarey, R. F. Hubbard, W. P. Leemans, A. Ting, and P. Sprangle, *Phys. Rev. Lett.* **79**, 2682 (1997).
- ¹⁰I. Kostyukov, A. Pukhov, and S. Kiselev, *Phys. Plasmas* **11**, 5256 (2004).
- ¹¹A. Sävert, S. P. D. Mangles, M. Schnell, E. Siminos, J. M. Cole, M. Leier, M. Reuter, M. B. Schwab, M. Möller, K. Poder, O. Jäckel, G. G. Paulus, C. Spielmann, S. Skupin, Z. Najmudin, and M. C. Kaluza, *Phys. Rev. Lett.* **115**, 055002 (2015).
- ¹²J. Faure, C. Rechatin, A. Norlin, A. Lifschitz, Y. Glinec, and V. Malka, *Nature (London)* **444**, 737–739 (2006).
- ¹³C. Rechatin, J. Faure, A. Ben-Ismaïl, J. Lim, R. Fitour, A. Specka, H. Videau, A. Tafzi, F. Burgy, and V. Malka, *Phys. Rev. Lett.* **102**, 164801 (2009).
- ¹⁴A. Pak, K. A. Marsh, S. F. Martins, W. Lu, W. B. Mori, and C. Joshi, *Phys. Rev. Lett.* **104**, 025003 (2010).
- ¹⁵C. McGuffey, A. G. R. Thomas, W. Schumaker, T. Matsuoka, V. Chvykov, F. J. Dollar, G. Kalintchenko, V. Yanovsky, A. Maksimchuk, K. Krushelnick, V. Y. Bychenkov, I. V. Glazyrin, and A. V. Karpeev, *Phys. Rev. Lett.* **104**, 025004 (2010).
- ¹⁶C. G. R. Geddes, K. Nakamura, G. R. Plateau, C. Toth, E. Cormier-Michel, E. Esarey, C. B. Schroeder, J. R. Cary, and W. P. Leemans, *Phys. Rev. Lett.* **100**, 215004 (2008).
- ¹⁷A. J. Gonsalves, K. Nakamura, C. Lin, D. Panasenkov, S. Shiraishi, T. Sokollik, C. Benedetti, C. B. Schroeder, C. G. R. Geddes, J. van Tilborg, J. Osterhoff, E. Esarey, C. Toth, and W. P. Leemans, *Nat. Phys.* **7**, 862–866 (2011).
- ¹⁸W. T. Wang, W. T. Li, J. S. Liu, Z. J. Zhang, R. Qi, C. H. Yu, J. Q. Liu, M. Fang, Z. Y. Qin, C. Wang, Y. Xu, F. X. Wu, Y. X. Leng, R. X. Li, and Z. Z. Xu, *Phys. Rev. Lett.* **117**, 124801 (2016).
- ¹⁹S. Bulanov, N. Naumova, F. Pegoraro, and J. Sakai, *Phys. Rev. E* **58**, R 5257 (1998).
- ²⁰K. Schmid, A. Buck, C. M. S. Sears, J. M. Mikhailova, R. Tautz, D. Herrmann, M. Geissler, F. Krausz, and L. Veisz, *Phys. Rev. Spec. Top. Accel. Beams* **13**, 091301 (2010).
- ²¹A. Buck, J. Wenz, J. Xu, K. Khrennikov, K. Schmid, M. Heigoldt, J. M. Mikhailova, M. Geissler, B. Shen, F. Krausz, S. Karsch, and L. Veisz, *Phys. Rev. Lett.* **110**, 185006 (2013).
- ²²S. Chou, J. Xu, K. Khrennikov, D. E. Cardenas, J. Wenz, M. Heigoldt, L. Hofmann, L. Veisz, and S. Karsch, *Phys. Rev. Lett.* **117**, 144801 (2016).
- ²³J. S. Liu, C. Q. Xia, W. T. Wang, H. Y. Lu, C. Wang, A. H. Deng, W. T. Li, H. Zhang, X. Y. Liang, Y. X. Leng, X. M. Lu, C. Wang, J. Z. Wang, K. Nakajima, R. X. Li, and Z. Z. Xu, *Phys. Rev. Lett.* **107**, 035001 (2011).
- ²⁴B. B. Pollock, C. E. Clayton, J. E. Ralph, F. Albert, A. Davidson, L. Divol, C. Filip, S. H. Glenzer, K. Herpoldt, W. Lu, K. A. Marsh, J. Meinecke, W. B. Mori, A. Pak, T. C. Rensink, J. S. Ross, J. Shaw, G. R. Tynan, C. Joshi, and D. H. Froula, *Phys. Rev. Lett.* **107**, 045001 (2011).
- ²⁵H. P. Schlenvoigt, K. Haupt, A. Debus, F. Budde, O. Jäckel, S. Pfotenhauer, H. Schwoerer, E. Rohwer, J. G. Gallacher, E. Brunetti, R. P. Shanks, S. M. Wiggins, and D. A. Jaroszynski, *Nat. Phys.* **4**, 130–133 (2008).
- ²⁶N. D. Powers, I. Ghebregziabher, G. Golovin, C. Liu, S. Chen, S. Banerjee, J. Zhang, and D. P. Umstadter, *Nat. Photonics* **8**, 28–31 (2013).
- ²⁷K. Khrennikov, J. Wenz, A. Buck, J. Xu, M. Heigoldt, L. Veisz, and S. Karsch, *Phys. Rev. Lett.* **114**, 195003 (2015).
- ²⁸J. A. Stamper and B. H. Ripin, *Phys. Rev. Lett.* **34**, 138 (1975).
- ²⁹M. C. Kaluza, H. P. Schlenvoigt, S. P. D. Mangles, A. G. R. Thomas, A. E. Dangor, H. Schwoerer, W. B. Mori, Z. Najmudin, and K. M. Krushelnick, *Phys. Rev. Lett.* **105**, 115002 (2010).
- ³⁰G. S. Settles, *Schlieren and Shadowgraph Techniques* (Springer, 2001).
- ³¹C. W. Siders, S. P. L. Blanc, D. Fisher, T. Tajima, M. C. Downer, A. Babine, A. Stepanov, and A. Sergeev, *Phys. Rev. Lett.* **76**, 3570 (1996).
- ³²A. Buck, M. Nicolai, K. Schmid, C. M. S. Sears, A. Sävert, J. M. Mikhailova, F. Krausz, M. C. Kaluza, and L. Veisz, *Nat. Phys.* **7**, 543 (2011).
- ³³D. Herrmann, L. Veisz, R. Tautz, F. Tavella, K. Schmid, V. Pervak, and F. Krausz, *Opt. Lett.* **34**, 2459 (2009).
- ³⁴C. M. S. Sears, A. Buck, K. Schmid, J. Mikhailova, F. Krausz, and L. Veisz, *Phys. Rev. ST Accel. Beams* **13**, 092803 (2010).
- ³⁵M. Wen, B. Shen, X. Zhang, F. Wang, Z. Jin, L. Ji, W. Wang, J. Xu, and K. Nakajima, *New J. Phys.* **12**, 045010 (2010).
- ³⁶F. Y. Li, Z. M. Sheng, Y. Liu, J. Meyer-ter-Vehn, W. B. Mori, W. Lu, and J. Zhang, *Phys. Rev. Lett.* **110**, 135002 (2013).
- ³⁷C. Nieter and J. R. Cary, *J. Comput. Phys.* **196**, 448 (2004).